Applied Physics Express 16, 055002 (2023)
https://doi.org/10.35848/1882-0786/acd0f2

LETTER

# Vortex structure in relaxed $BaTiO_3/SrTiO_3$ superlattice

Fengjuan Yang[1,2], Yongfeng Liang[3], and Pingping Wu[1,2*]

[1]Department of Materials Science and Engineering, Xiamen Institute of Technology, Xiamen, Fujian 361021, People's Republic of China
[2]The Higher Educational Key Laboratory for Flexible Manufacturing Equipment Integration of Fujian Province, Xiamen Institute of Technology, Xiamen, Fujian 361021, People's Republic of China
[3]State Key Laboratory for Advanced Metals and Materials, University of Science and Technology Beijing, Beijing, 100083, People's Republic of China

*E-mail: pingpingwu@xit.edu.cn; pingpingwu-ustb@126.com

Received March 17, 2023; revised April 23, 2023; accepted April 27, 2023; published online May 11, 2023

In this work, using the phase-field model, we demonstrated vortex structure can be generated in a lead-free $BaTiO_3/SrTiO_3$ superlattice structure. The labyrinth pattern (maze-like) domain structure was observed in a fully relaxed $BaTiO_3/SrTiO_3$ superlattice structure. Topological bubble-like rosette structures were found at an out-of-plane field, and polar skyrmions were obtained after the electric field was removed. In a designed fully relaxed nanowire of width ∼8 nm, near-perfect periodical clockwise-counterclockwise ferroelectric vortex pairs were generated due to the interfacial constraints. The simulated topological structures are potentially relevant to the application of high-density ferroelectrics memory devices.


Over the last decade, an increasing number of topological ferroelectric structures have been discovered through theoretical predictions and experimental observations.[1–14] In particular, the vortex structure discovered in $PbTiO_3$(PT)/$SrTiO_3$(ST) superlattices has garnered significant attention because of its potential applications in ferroelectric memory devices and other various dielectric/ferroelectric applications.[15–26] However, the Pb contained in $PbTiO_3$ is not environmentally friendly. A superlattice with $PbTiO_3$ has been constructed, which relies on the fact that $PbTiO_3$ exhibits extremely high spontaneous polarization at room temperature and that the interfacial coherence between the substrate/film and the superlattice material can significantly affect the ferroelectric structure and properties of the superlattice. This is concluded based on the strain–temperature phase diagrams of $PbTiO_3$ and $SrTiO_3$ and the lattice parameters of ferroelectrics.[27] Yadav et al.[18] grew a $PbTiO_3$ (lattice parameter $a$ = 3.9547 Å)/$SrTiO_3$ ($a$ = 3.905 Å) superlattice on a $DyScO_3$ substrate ($a$ = 3.945 Å[28]), which caused the $PbTiO_3$ phase to be in a small biaxial compressive constrained state and in the tetragonal phase (constraint strain of ∼0.22%), and the $SrTiO_3$ phase under tensile constraint (∼1.013%) but not reaching the ferroelectric transition point. Under such elastic constraint conditions, the $PbTiO_3$ layer separated by two paraelectric phases remains in an approximately strain-free state, thereby resulting in a vortex structure owing to electrostatic interactions and size effects.

We believe that a structure similar to other superlattice structures should be designed to avoid the use of the toxic element Pb. Owing to the ultrahigh degrees of freedom of the superlattice structure, an appropriate superlattice structure can be designed by regulating the substrate, stacking structure, and temperature to achieve certain properties. Theoretically, an infinite number of stacking structures exist at ambient temperature, which allows our requirements to be satisfied.

The aim of this study is to investigate the possibility of achieving similar vortex structures in Pb-free superlattice structures. In this study, we employed $BaTiO_3$(BT)/$SrTiO_3$(ST) structures because of their strong ferroelectricity, tunable Curie temperatures, and pertinence to various applications.[29–35] We first investigated the ferroelectric domain structures of BT/ST superlattices grown on a $DyScO_3$ substrate; subsequently, we examined the fully relaxed superlattice structure $BT_6/ST_8$ and observed vortices at the cross-sectional plane. The generated maze- and labyrinth-like structures can be transformed into bubble-like structures under a certain electric field. Using the concept of "race-trace" memory devices, which limit the ferroelectric body to one-dimensional nanowires, clockwise (CW) and counterclockwise (CCW) vortex pairs were clearly observed in our simulation. Our simulation indicates a possible method for creating and designing a similar vortex structure in ferroelectric superlattices, which presents high potential for application in ferroelectric memory devices.

To simulate a ferroelectric superlattice structure, we selected a parameter $\eta$ to distinguish between the BT and ST phases. In the simulation, $\eta(r) = 1$ and $\eta(r) = 0$ indicate that position r is occupied by ferroelectric BT and paraelectric ST phases, respectively; and $\eta$ was set to 0.5 at the interface. The order parameter field describing the ferroelectric domain state is the spontaneous polarization $P_i$ ($i = 1$, 2, and 3). For the multilayered superlattice structure, periodic boundary conditions were employed in the $x-$, $y-$, and $z$-directions. The effect of the substrate on the epitaxially strained superlattice was introduced through the elastic energy.

According to the Ginzburg–Landau theory, the total energy of a superlattice is expressed as

$$\begin{aligned}F_{\text{tot}} &= \int_V (f_{\text{bulk}} + f_{\text{inter}} + f_{\text{elec}} + f_{\text{elas}})dV\\ &= \int_V [\alpha_i P_i^2 + \alpha_{ij} P_i^2 P_j^2 + \alpha_{ijk} P_i^2 P_j^2 P_k^2\\ &+ \alpha_{ijkl} P_i^2 P_j^2 P_k^2 P_l^2 + \frac{1}{2}\gamma_{ijkl}\frac{\partial P_i}{\partial x_j}\frac{\partial P_k}{\partial x_l}\\ &- \frac{1}{2}\varepsilon_b\varepsilon_0 E_i^2 - E_i P_i + \frac{1}{2}C_{ijkl}\\ &\times (\varepsilon_{ij} - Q_{ijkl}P_k P_l)(\varepsilon_{kl} - Q_{klij}P_i P_j)]dV, \qquad (1)\end{aligned}$$

where $f_{\text{bulk}}$, $f_{\text{inter}}$, $f_{\text{elec}}$, and $f_{\text{elas}}$ represent the bulk free, interfacial, electrostatic, and elastic energies, respectively; $V$ is the total volume; Einstein's summation rule and Voigt's matrix notation are employed for the tensors; $\alpha_i$, $\alpha_{ij}$, $\alpha_{ijk}$, and $\alpha_{ijkl}$ are the Landau expansion coefficients for bulk energy; $\gamma_{ijkl}$ is the gradient energy coefficient; $\varepsilon_b$ and $\varepsilon_0$ are the background dielectric constant and vacuum permittivity, respectively; and $E_i$ is the external electric field. Khachaturyan's elastic theory[36] and high-order approximations[37] were used to calculate the elastic energy of the elastic inhomogeneous system. $C_{ijkl}$ and $Q_{ijkl}$ denote the elastic stiffness and electrostrictive coefficient tensors, respectively, and $\varepsilon_{ij}$ is the total strain.

The Landau coefficients, elastic coefficients, and electrostrictive coefficients for the superlattice system can be expressed in the following form:

$$\alpha_1(r) = \eta(r) \times \alpha_1(\mathrm{BT}) + (1 - \eta(r)) \times \alpha_1(\mathrm{ST}). \quad (2)$$

Therefore, for the BT and ST phases, $\alpha_1 = \alpha_1(\mathrm{BT})$ and $\alpha_1 = \alpha_1(\mathrm{ST})$, whereas for the interface region, $\alpha_1 = 0.5(\alpha_1(\mathrm{BT}) + \alpha_1(\mathrm{ST}))$. All the corresponding values of the coefficients used in this study are available in our previous publications.[38,39]

The spatial variation in ferroelectric polarization is governed by the time-dependent Ginzburg–Landau equation as follows:

$$\frac{\partial \mathbf{P_i}(\boldsymbol{r}, \boldsymbol{t})}{\partial \mathrm{t}} = -L\frac{\delta \mathrm{F_{tot}}}{\delta \mathbf{P_i}(\boldsymbol{r}, \boldsymbol{t})}, \quad (3)$$

where $L$ is the dynamic coefficient and $t$ is time. In our simulation, $\eta$ was considered static for simplicity.

A schematic illustration of the superlattice structure is shown in Fig. 1(a). As shown in the figure, a periodic stacking structure of the superlattice $(\mathrm{BaTiO_3})_m/(\mathrm{SrTiO_3})_n$ was epitaxially grown on a certain substrate layer-by-layer, where m and n represent the unit cell thickness. The ferroelectric properties of the superlattice were significantly affected by its underlying substrate, which was attributed to the biaxial in-plane strain controlled by the lattice mismatch between the superlattice and substrate. When the superlattice structure was completely commensurately grown on the $\mathrm{SrTiO_3}$ substrate at room temperature [Fig. 1(b)], the ST layer remained paraelectric in the unstrained state, whereas the BT layer exhibited ferroelectricity and was affected by compressive strain because the lattice parameter of BT (~4.008 Å) is larger than that of the substrate ST (~3.905 Å). For a ferroelectric thin-film structure, the strain-relaxation process between the thin film and substrate

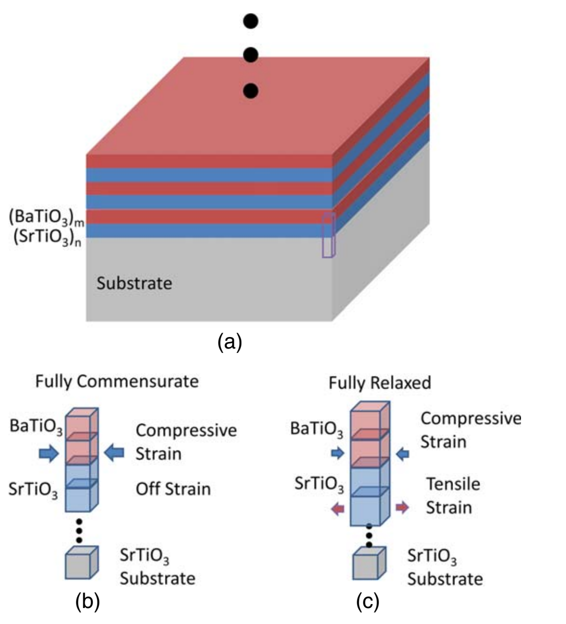


**Fig. 1.** (a) A schematic plot of $\mathrm{BT}_m/\mathrm{ST}_n$ superlattice structure. (b) Strain condition in BT/ST layer when superlattice is fully commensurate grown on $\mathrm{SrTiO_3}$ substrate. (c) Under fully relaxed conditions, the BT layer suffered from compressive strain while the ST layer suffers a tensile strain.

alters the biaxial in-plane strain. For example, when the BT/ST superlattice was fully relaxed, the effect of the substrate was negligible, and the superlattice relied on its structure to balance the mismatch strain. In this case, the superlattice was relaxed to the average values of the lattice parameters of the ST and BT layers. As shown in Fig. 1(c), the ST layer was constrained by a biaxial tensile stress, whereas the BT layer was constrained by a biaxial compressive stress. Based on our previous study,[39] tetragonal c+/c− domains can be observed in the BT layer, and the ST layer remains in an orthorhombic phase and acquires in-plane polarization, which has been similarly confirmed in experimental studies.[40,41]

To obtain vortex structures in Pb-free BT/ST superlattices, we first investigated the role of the stacking structure on the ferroelectric domain patterns using an appropriate substrate. The $\mathrm{DyScO_3}$ substrate was used at the beginning of the study as it features an in-plane lattice parameter of 3.945 Å, which is similar to the average value of the lattice parameters of BT and ST, and is frequently used for the growth of PT/ST superlattice heterostructures. We systematically examined changes in the domain structure by regulating the thicknesses of the BT and ST layers. In the phase-field model, we first changed the thickness of the ST layer while fixing the thickness of the BT layer fixed; subsequently, we changed the thickness of the BT layer while fixing the thickness of the ST layer. Figure 2 illustrates the systematic phase-field prediction of the ferroelectric domain structure of $\mathrm{BT}_m/\mathrm{ST}_n$ ($m$, $n$ = 4, 6, 8, and 10), which was completely commensurately grown on the $\mathrm{DyScO_3}$ substrate. The simulation was performed with grids measuring $32\Delta x \times 32\Delta y \times (m + n)\Delta z$, where $\Delta x = \Delta y = 1$ nm and $\Delta z \sim 0.4$ nm. Similar stable domain patterns were obtained by changing the initial random values or using a lattice phase-field model.[42] Because the interface-intermixing effect was considered in the simulation, we examined domain structures with one and no intermixing layers. The simulation results showed that interface intermixing did not significantly affect the polarization and domain structure.

In the case involving an ultrathin layer ($m$, $n$ <= 3), the phase-field model indicated negligible polarization in the BT layers owing to the interfacial and electrostatic interactions, which is consistent with the result of a previous study.[19] A tetragonal c+/c− domain structure with polarization in the +/−$z$-direction was observed in the BT phase owing to the compressive strain at the substrate and BT/ST interface. The polarization in the BT layer was insufficient for the $\mathrm{BT}_4/\mathrm{ST}_n$ structures, whereas that in the ST layer increased owing to tensile biaxial strain. Additionally, in-plane polarization was observed in the ST layer of the superlattice $\mathrm{BT}_4/\mathrm{ST}_{10}$ structure, which is consistent with the experimental measurements. A labyrinth (maze-like) pattern[43] emerged in the BT layer, which reduced the electrostatic energy. As the layer thickness of the paraelectric phase increased, the ferroelectric domain size decreased, and the domain wall boarded. Meanwhile, induced polarization was observed along the $z$-direction in the ST layer of the $\mathrm{BT}_8/\mathrm{ST}_4$ and $\mathrm{BT}_{10}/\mathrm{ST}_4$ structures, which reduced the depolarization of the electric field. As the thickness of the ST layer increased, the polarization in the ST layer switched from the out-of-plane direction to the in-plane direction. By contrast, when the ST layer thickness exceeded 6, the domain structure of the BT

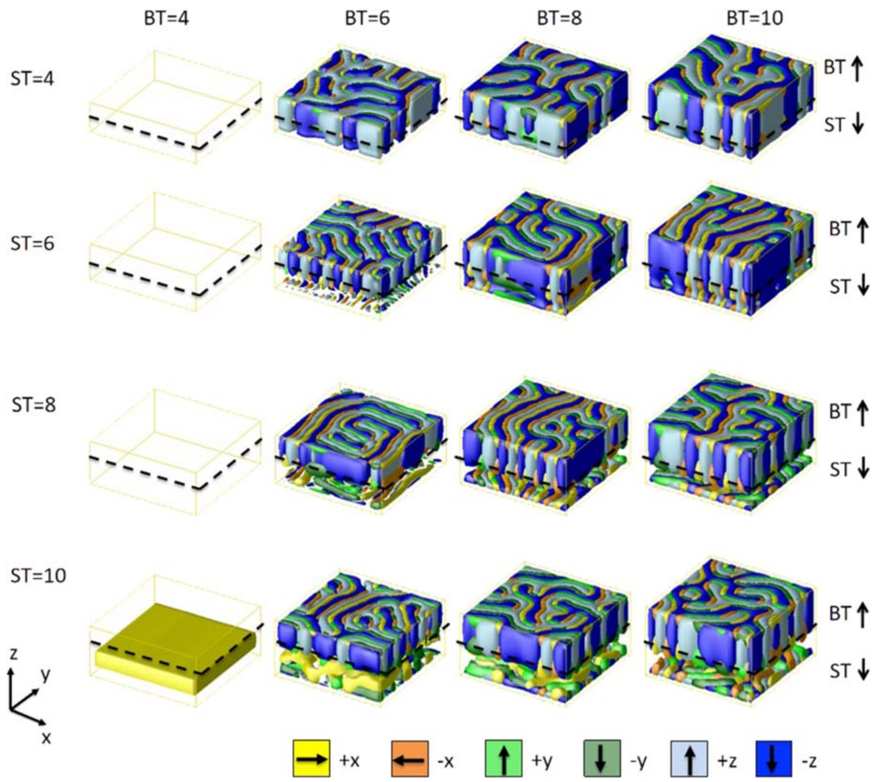


**Fig. 2.** Ferroelectric domain patterns for $BT_m/ST_n$ ($m$, $n$ = 4, 6, 8, 10) fully commensurate grown on $DyScO_3$ substrate.

layer changed slightly as the thickness of the ST layer increased.

Based on the simulation results illustrated in Fig. 2, the BT layer remained in a compressively constrained state at all times. Therefore, if vortex structures are created in this state, then thinner BT layers are favored; otherwise, a flux-closure structure may form in the BT layer. To amplify the interface constraint behavior for creating a vortex structure, the ST layer should be sufficiently thick such that the ST layer evolves into a paraelectric state and can be effectively used to separate the ferroelectric layers. We selected $BT_6/ST_8$ as the target structure and placed it in a relaxed state. The relaxed superlattice structure was more stable and had an average lattice constant equivalent to that of the $DyScO_3$ substrate. We examined the ferroelectric domain patterns of the fully relaxed superlattice structure of $BT_6/ST_8$ with an average lattice parameter of 3.945 Å, as shown in Fig. 3(a). A larger simulation grid measuring $64\Delta x \times 64\Delta y \times 14\Delta z$ was employed, where $\Delta x = \Delta y = 1$ nm, and $\Delta z \sim 0.4$ nm. In the cross-sectional vector plots [Fig. 3(b)], we clearly observed CW–CCW vortex pairs and in-plane polarization arising from the effect of the paraelectric/ferroelectric interface. The cross-sectional plane was not perpendicular to the $+c/-c$ domain wall because a labyrinthine domain structure was generated in the simulation.

Because the thickness ratio of BT/ST is a key parameter for controlling the ferroelectric properties of the superlattice, the domain patterns of the superlattice structures of $BT_{16}/ST_8$ and $BT_{32}/ST_8$ were examined via phase-field simulations, as shown in Figs. 3(c) and 3(d), respectively. All the domain patterns were labyrinth-like, and a continuous transition from a vortex structure to a flux-closed structure appeared in the cross-sectional plane vector plot. The transverse dimension of the labyrinth stripe domain increased with the thickness of the BT layer. Based on the vortex critical aspect ratio criterion of $r \sim 0.3$, as suggested by Hong et al.,[19] the upper limit for the $BT_m/ST_8$ superlattice is $m \sim 16$, above which the vortex structure can be regarded as a 180° domain wall. To estimate the lower limit for the labyrinth domain, the fully relaxed superlattice structure of $BT_4/ST_8$ with an average lattice parameter of 3.937 Å was simulated; consequently, a paraelectric phase was observed in the superlattice structure. Based on the discussion above, the lower and upper bounds of the BT/ST thickness ratio for observing the vortex structure and labyrinth domains were set to 0.75:1($BT_6/ST_8$) and 2:1($BT_{16}/ST_8$), respectively.

The fully relaxed BT/ST structure exhibited a maze-like domain structure analogous to the maze domains in the magnetic thin films of uniaxial ferrite materials. For such magnetic materials, the maze-like domains transform into magnetic bubble domains when the magnetic field perpendicular to the film surface is increased. By applying an electric field of $2.9 \times 10^7$ V m$^{-1}$ in the $+z$–/$-z$-direction perpendicular to the $BT_6/ST_8$ superlattice thin film plane, a similar bubble-like structure was generated in the simulation, as shown in Fig. 4(a). The bubble structure in ultrathin BT films has been predicted using first-principles technology.[44] Figure 4(b) shows a top view of the vector distribution in the red box in Fig. 4(a). The rosette structure in the domain structure and the "hedgehog" configuration in the vector plots are clearly shown in the figure.[4] The planar dimensions of these bubble configurations were 3–7 nm, thus forming a hexagonal bubble lattice. The simulation results showing a phase stability sequence of labyrinth→bubbles→monodomain were consistent with the experimental results. Recent studies pertaining to similar ferroelectric bubble structures

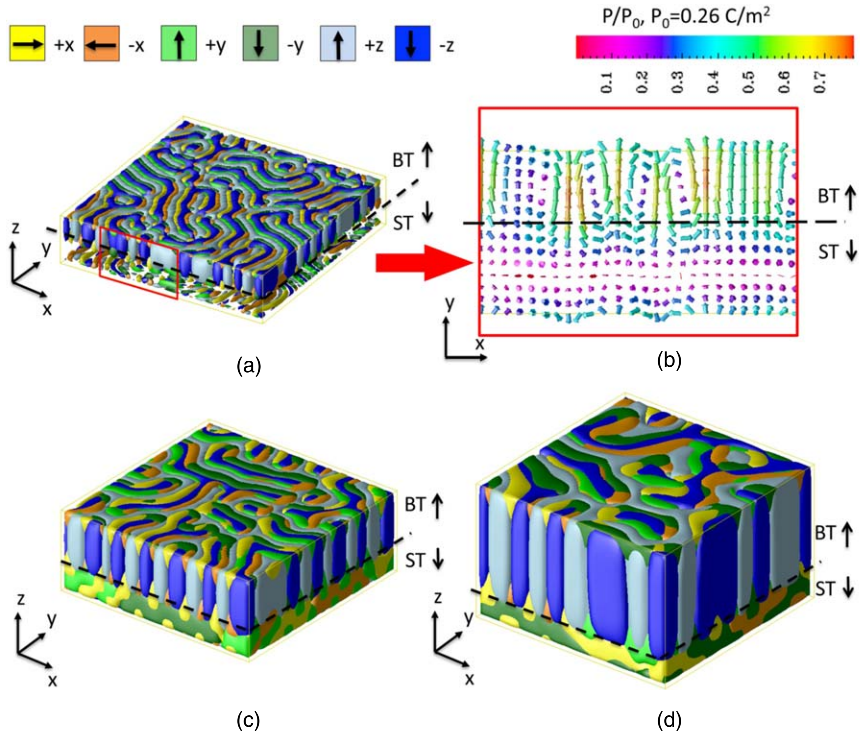


Fig. 3. (a) Domain structure of fully relaxed superlattice $BT_6/ST_8$. (b) polarization vector plots for the cross-section plane of $BT_6/ST_8$. (c), (d) Domain structure of fully relaxed superlattice $BT_{16}/ST_8$ and $BT_{32}/ST_8$.

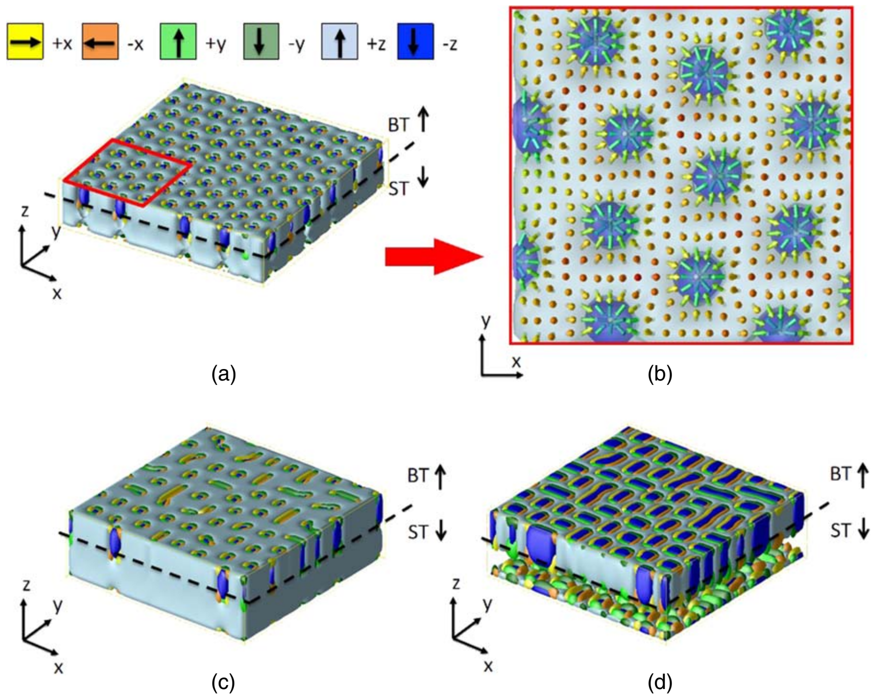


Fig. 4. (a) Bubble-like domains in $BT_6/ST_8$ superlattice structure at a field of $2.9 \times 10^7$ V m$^{-1}$ along the z-direction. (b) The top view of vector plots shows rosette-like patterns and hexagonal matrix arrays. (c) The simulated bubble-like domain structure of $BT_9/ST_{12}$ superlattice at an external field of $8.69 \times 10^7$ V m$^{-1}$. (d) The skyrmion structure is demonstrated when the applied field is removed.

suggest that topological bubbles formed in ferroelectric superlattice structures can result in certain processes in bubble-based ferroelectric devices.[4,6,9,10,12,14] However, the predicted ferroelectric bubble domains ($\sim$5 nm) were significantly smaller than the ferromagnetic bubbles (>50 nm in diameter);[45] therefore, a much faster operation speed can be achieved for memory or logic device applications. Meanwhile, as the thickness of the BT and ST layers increased, similar bubble-like structures were achieved at a larger electric field of $8.69 \times 10^7$ V m$^{-1}$ in the fully relaxed $BT_9/ST_{12}$ superlattice structure, as shown in Fig. 4(c). After removing the electric field, the residual bubble structures expanded and became stable polar skyrmions, as shown in Fig. 4(d).

IBM researchers have developed a new storage concept for devices by exploiting domain wall shift. Racetrack memory

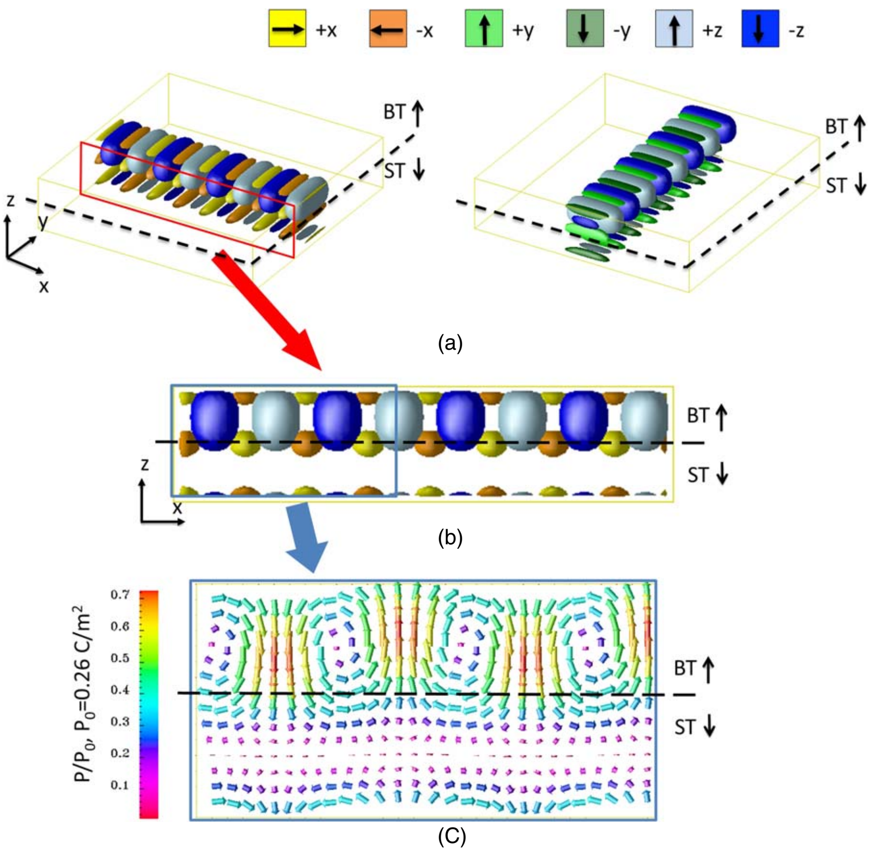


**Fig. 5.** (a) Simulated $BT_6/ST_8$ nanowires along *x*/*y* directions. (b) A cross-sectional plot of the domain structure. (c) Vector plots show periodical CW/CCW vortex pairs in the BT layer.

devices,[46] which are one-dimensional magnetic nanowire devices, has caused to consider the possibility of creating analogous ferroelectric devices by placing ferroelectric structures in a one-dimensional limit. Figure 5 shows the lattice phase-field simulation[42] results of the $BT_6/ST_8$ superlattice nanowire based on a $20 \times 64 \times 14$ mesh grid and a transverse size of approximately 8 nm. The nanowire was arranged periodically in the *z*-direction during the simulation. CW/CCW vortex pairs were observed in the nanowire structure owing to electrostatic interactions, as shown in Fig. 5(a). A detailed cross-sectional plot of the vortex domains and the distribution of the polarization vectors are shown in Figs. 5(b) and 5(c). Near-perfect vortex pairs were generated in the Pb-free BT/ST nanowire structures under fully relaxed constraint conditions. Additionally, a rectangular instead of a square vortex structure was observed because of the in-plane straining of the film. This structure offers the possibility of enhancing high-density bit-memory applications.

In this study, we simulated the ferroelectric domains of $BT_m/ST_n$ superlattice structures grown on $DyScO_3$ substrates at room temperature. Under ambient conditions, labyrinth domain structures and CW/CCW vortex polarization pairs were obtained in the BT layer of the fully relaxed superlattice structure $BT_6/ST_8$. A three-dimensional nanobubble structure emerged under an out-of-plane electric field. Polar skyrmion structures were observed in the fully relaxed $BT_9/ST_{12}$ superlattice structure after the removal of an electric field measuring $8.69 \times 10^7$ V m$^{-1}$. The phase-field simulation results indicated the possibility of forming similar vortex structures in multilayered BT/ST nanowires. In the future, we plan to conduct experiments that involve changing the thickness and geometric structure of the BT/ST superlattice heterostructure.

**Acknowledgments** This work was supported by the Advanced Functional Materials Research and Innovation Group of Xiamen Institute of Technology (Grant No. KYTD202004) and the State Key Lab of Advanced Metals and Materials of the University of Science and Technology Beijing (Grant No. 2021-ZD02).

**ORCID iDs** Pingping Wu https://orcid.org/0000-0002-7240-3760


1) C. Back et al., J. Phys. D: Appl. Phys. **53**, 363001 (2020).
2) Z. Li et al., Sci. Adv. **3**, e1700919 (2017).
3) S. Yuan, W. Chen, J. Liu, Y. Liu, B. Wang, and Y. Zheng, J. Phys. Condens. Matter **30**, 465304 (2018).
4) S. Das et al., Nature **568**, 368 (2019).
5) N. Strkalj, E. Gradauskaite, J. Nordlander, and M. Trassin, Materials (Basel) **12**, 3108 (2019).
6) G. Tian, W. Yang, D. Chen, Z. Fan, Z. Hou, M. Alexe, and X. Gao, Natl. Sci. Rev. **6**, 684 (2019).
7) S. Das, Z. Hong, M. McCarter, P. Shafer, Y.-T. Shao, D. A. Muller, L. W. Martin, and R. Ramesh, APL Mater. **8**, 120902 (2020).
8) Y. J. Wang et al., Nat. Mater. **19**, 881 (2020).
9) S. R. Bakaul, S. Prokhorenko, Q. Zhang, Y. Nahas, Y. Hu, A. Petford-Long, L. Bellaiche, and N. Valanoor, Adv. Mater. **33**, e2105432 (2021).
10) S. Chen et al., Adv. Mater. **33**, e2000857 (2021).
11) S. Das et al., Nat. Mater. **20**, 194 (2021).
12) J. Yin et al., Nat. Commun. **12**, 3632 (2021).
13) P. Behera et al., Sci. Adv. **8**, eabj8030 (2022).
14) V. Govinden, S. Rijal, Q. Zhang, Y. Nahas, L. Bellaiche, N. Valanoor, and S. Prokhorenko, Phys. Rev. Mater. **7**, L011401 (2023).
15) H. Aramberri, N. S. Fedorova, and J. Iniguez, Sci. Adv. **8**, eabn4880 (2022).
16) A. Gruverman, D. Wu, H. J. Fan, I. Vrejoiu, M. Alexe, R. J. Harrison, and J. F. Scott, J. Phys. Condens. Matter **20**, 342201 (2008).
17) P. Zubko, J. C. Wojdel, M. Hadjimichael, S. Fernandez-Pena, A. Sene, I. Luk'yanchuk, J. M. Triscone, and J. Iniguez, Nature **534**, 524 (2016).


 

18) A. K. Yadav et al., Nature **530**, 198 (2016).
19) Z. Hong et al., Nano Lett. **17**, 2246 (2017).
20) D. Karpov, Z. Liu, T. D. S. Rolo, R. Harder, P. V. Balachandran, D. Xue, T. Lookman, and E. Fohtung, Nat. Commun. **8**, 280 (2017).
21) Q. Li, C. T. Nelson, S. L. Hsu, A. R. Damodaran, L. L. Li, A. K. Yadav, M. McCarter, L. W. Martin, R. Ramesh, and S. V. Kalinin, Nat. Commun. **8**, 1468 (2017).
22) W. J. Chen, S. Yuan, L. L. Ma, Y. Ji, B. Wang, and Y. Zheng, RSC Adv. **8**, 4434 (2018).
23) S. L. Hsu, M. R. McCarter, C. Dai, Z. Hong, L. Q. Chen, C. T. Nelson, L. W. Martin, and R. Ramesh, Adv. Mater. **31**, e1901014 (2019).
24) Z. Hong, S. Das, C. Nelson, A. Yadav, Y. Wu, J. Junquera, L. Q. Chen, L. W. Martin, and R. Ramesh, Nano Lett. **21**, 3533 (2021).
25) Q. Li et al., Nature **592**, 376 (2021).
26) C. Tan et al., Nat. Commun. **12**, 4620 (2021).
27) D. G. Schlom, L.-Q. Chen, C.-B. Eom, K. M. Rabe, S. K. Streiffer, and J.-M. Triscone, Annu. Rev. Mater. Res. **37**, 589 (2007).
28) A. Soukiassian et al., J. Mater. Res. **23**, 1417 (2011).
29) D. A. Tenne et al., Science **313**, 1614 (2006).
30) Y. Liu and X.-P Peng, Appl. Phys. Express **5**, 011501 (2012).
31) V. Železný, A. Soukiassian, D. G. Schlom, and X. X. Xi, J. Appl. Phys. **115**, 184102 (2014).
32) O. F. Shoron, S. Raghavan, C. R. Freeze, and S. Stemmer, Appl. Phys. Lett. **110**, 232902 (2017).
33) S. Estandia, F. Sanchez, M. F. Chisholm, and J. Gazquez, Nanoscale. **11**, 21275 (2019).
34) Z. Wang, H. Cao, Q. Liu, Z. Cui, H. Xu, H. Zhou, X. Zhai, and Y. Lu, J. Phys. D: Appl. Phys. **53**, 314004 (2020).
35) H. Itasaka, K.-I Mimura, K. Yasui, K. Hamamoto, and K. Kato, Appl. Phys. Express **15**, 095002 (2022).
36) A. G. Khachaturyan, *Theory of Structural Transformations In Solids* (Wiley, New York, 1983).
37) S. Y. Hu and L. Q. Chen, Acta Mater. **49**, 1879 (2001).
38) P. Wu, X. Ma, Y. Li, V. Gopalan, and L.-Q. Chen, Appl. Phys. Lett. **100**, 092905 (2012).
39) P. Wu, X. Ma, Y. Li, C.-B. Eom, D. G. Schlom, V. Gopalan, and L.-Q. Chen, Appl. Phys. Lett. **107**, 122906 (2015).
40) A. Q. Jiang, J. F. Scott, Hb Lu, and Z.-h Chen, J. Appl. Phys. **93**, 1180 (2003).
41) S. Ríos, A. Ruediger, A. Q. Jiang, J. F. Scott, Hb Lu, and Z.-B. Chen, J. Phys. Condens. Matter **15**, L305 (2003).
42) P. Wu and Y. Liang, Materials **14**, 7317 (2021).
43) A. N. Morozovska, E. A. Eliseev, Y. M. Fomichov, Y. M. Vysochanskii, V. Y. Reshetnyak, and D. R. Evans, Acta Mater. **183**, 36 (2020).
44) B.-K. Lai, I. Ponomareva, I. A. Kornev, L. Bellaiche, and G. J. Salamo, Phys. Rev. B **75**, 085412 (2007).
45) T. H. O'dell, Rep. Prog. Phys. **49**, 589 (1986).
46) S. S. Parkin, M. Hayashi, and L. Thomas, Science **320**, 190 (2008).